Knotting fractional-order knots with the polarization state of light

Emilio Pisanty[1*], Gerard J. Machado[1], Verónica Vicuña-Hernández[1], Antonio Picón[1,2], Alessio Celi[1,3,4,5], Juan P. Torres[1,6] and Maciej Lewenstein[1,7]

[1] ICFO – Institut de Ciencies Fotoniques, The Barcelona Institute of Science and Technology, Av. Carl Friedrich Gauss 3, 08860 Castelldefels (Barcelona), Spain
[2] Departamento de Química, Universidad Autónoma de Madrid, 28049, Madrid, Spain
[3] Center for Quantum Physics, University of Innsbruck, Innsbruck, Austria
[4] Institute for Quantum Optics and Quantum Information, Austrian Academy of Sciences, Innsbruck, Austria
[5] Departament de Física, Universitat Autònoma de Barcelona, E-08193 Bellaterra, Spain
[6] Department of Signal Theory and Communications, Universitat Politecnica de Catalunya, Barcelona, Spain
[7] ICREA, Passeig de Lluís Companys, 23, 08010 Barcelona, Spain

*emilio.pisanty@icfo.eu

10 June 2019
This is the Accepted Manuscript for *Nature Photonics* **13**, 569 (2019), arXiv:1808.05193.

The fundamental polarization singularities of monochromatic light are normally associated with invariance under coordinated rotations: symmetry operations that rotate the spatial dependence of an electromagnetic field by an angle θ and its polarization by a multiple $\gamma\theta$ of that angle. These symmetries are generated by mixed angular momenta of the form $J_\gamma = L + \gamma S$, and they generally induce Möbius-strip topologies, with the coordination parameter γ restricted to integer and half-integer values. In this work we construct beams of light that are invariant under coordinated rotations for arbitrary rational γ, by exploiting the higher internal symmetry of 'bicircular' superpositions of counter-rotating circularly polarized beams at different frequencies. We show that these beams have the topology of a torus knot, which reflects the subgroup generated by the torus-knot angular momentum J_γ, and we characterize the resulting optical polarization singularity using third-and higher-order field moment tensors, which we experimentally observe using nonlinear polarization tomography.

The past three decades have witnessed an explosion in our abilities to control the behaviour of light, and in our understanding of the possible structures and topologies of electromagnetic radiation [1–4]. Building on the initial discoveries of wavefront dislocations and phase singularities [5], the field of singular optics now spans from optical communication technology [6] through imaging [7], the mechanical manipulation of matter [8, 9] and XUV/x-ray applications [10], to a detailed understanding of the classical and quantum natures of the angular momentum of light [11–13].

Some of the most fascinating structures discovered by this programme are the topological features of light: recent work has described, sometimes experimentally, light fields with intricate knots in their field lines [14], optical vortices [15–17] and C-lines [18], as well as fields with spirals [19], umbilics [20, 21], ribbons [22] and Möbius strips [23–28] in their polarization, all of which give rise to rich spin-orbit photonics when coupled with space-dependent birefringent elements [29–31]. These structures are often associated with the invariance of the light field under coordinated rotations: that is, symmetry operations that rotate the spatial dependence of the fields by an angle θ and the fields' polarization by a multiple $\gamma\theta$ of that angle, which means that they are associated with 'mixed' angular momenta [32] of the form $L_z + \gamma S_z$, where L_z and S_z are the orbital and spin angular momenta of light about the symmetry axis; these are conserved separately within the paraxial approximation [11, 13], and can be measured independently [33, 34].

For monochromatic light, the rotation coordination parameter γ must be either an integer or a half-integer [20, 32], since the only internal symmetry of a polarization ellipse is a rotation by π over a half-period delay. However, general electromagnetic fields are not subject to this restriction: as a simple example, a three-fold rotational symmetry is possible by combining a circularly-polarized field with a counter-rotating second harmonic [35, 36], a configuration that forms a so-called 'bicircular' [37] trefoil-shaped Lissajous figure. The Lissajous singularities of bichromatic fields have been the object of some study [38–41], but their rotational properties have thus far largely gone unexplored.

In this work we use the higher internal symmetry of bicircular fields to construct and characterize beams of electromagnetic radiation that are invariant under coordinated rotations, as generated by $L_z + \gamma S_z$, for an arbitrary coordination parameter γ. Topologically, these beams' polarization corresponds to a torus knot, characterized by two indices: the order n of internal symmetry of the polarization Lissajous figure, and the number of internal-symmetry rotations produced by a spatial traversal around the central singularity; for each internal symmetry, the latter forms a topologically-protected winding number of the electromagnetic field.

Moreover, we show how this winding number arises naturally as the phase winding number of the multipolar components of the third- and higher-order field tensor moments $\langle E_i E_j \cdots E_k \rangle$, in analogy to the monochromatic polarization ellipse's appearance as the quadrupole component of the polarization matrix $\langle E_i E_j \rangle$. Finally, we experimentally demonstrate these torus-knot beams and characterize their winding number via nonlinear polarization tomography.

Coordinated-rotation invariance

For monochromatic light, rotational invariance is normally framed by requiring that the complex amplitude $\tilde{\mathbf{E}}(\mathbf{r})$ of the electric field obey an eigenvalue equation of the form

$$\hat{\mathcal{G}}\,\tilde{\mathbf{E}}(\mathbf{r}) = g\,\tilde{\mathbf{E}}(\mathbf{r}), \tag{1}$$

for some symmetry generator $\hat{\mathcal{G}}$. For polychromatic superpositions, however, there is no longer a single complex amplitude to which an eigenvalue equation like (1) can be applied – and indeed, if one looks for invariant states by applying the generator $\hat{\mathcal{G}} = \hat{L}_z + \gamma\hat{S}_z$ separately to each amplitude and asking for joint eigenstates, one becomes (erroneously) restricted to the conclusions of the monochromatic case.

To deal effectively with the rotational invariance of polychromatic beams, then, it is crucial to realize that, even in the monochromatic case, the real-valued physical field $\mathbf{E}(\mathbf{r},t) = \mathrm{Re}\left[\tilde{\mathbf{E}}(\mathbf{r})e^{-i\omega t}\right]$ is rarely an eigenstate of the symmetry generator. Instead, the rotational invariance of the physical force fields describes an equivalence between the symmetry operation and a time translation: for coordinated rotations, this reads

$$R(\gamma\alpha)\mathbf{E}\big(R^{-1}(\alpha)\mathbf{r},t\big) = \mathbf{E}(\mathbf{r},t+\tau\alpha), \tag{2}$$

where $R(\alpha)$ is a rotation matrix by angle α about the beam's symmetry axis, and τ is a constant with dimensions of time.

This invariance condition is fulfilled trivially by circularly-polarized orbital-angular-momentum beams [11], which are separately invariant under rotations of the image and the polarization. (Moreover, those rotations can be independently implemented when restricted to a single axis, using half-wave plates and Dove prisms, respectively [32].) Going beyond that, one can also form solutions of (2) which are invariant under the combined transformation but not under either of the separate ingredients: this is the case, for instance, for the 'lemon' and 'star' umbilic ellipse points [20, 21], as well as the flat Möbius bands produced by conical refraction [32]. These solutions require an integer or half-integer γ, since only rotations by multiples of π will return a monochromatic polarization ellipse to itself, and the fields can generally be decomposed as superpositions of circularly-polarized beams of different orbital angular momentum.

To generalize these beams, we look to bichromatic combinations with higher-order internal rotational symmetry in the polarization, as provided by the bicircular combination [37] shown in figure 1a: we superpose a right-handed circularly polarized (RCP) beam at a fundamental frequency $\omega_1 = \omega$ with its second harmonic at $\omega_2 = 2\omega$ on a left-circular polarization (LCP). Thus, over one-third of a period of the fundamental, the former rotates counter-clockwise by 120°, while the latter rotates clockwise by 240°, so the polarization combination is rotated rigidly by $2\pi/3$. More generally, combining counter-rotating beams at $\omega_1 = p\omega$ and $\omega_2 = q\omega$, for p, q coprime integers, will give a $(p+q)$-fold-symmetric Lissajous figure, but we focus on the ω-2ω combination for simplicity.

Finally, to extend this symmetry to coordinated rotations, we work as in the monochromatic case and give the two light fields at frequencies ω_1 and ω_2 different orbital angular momentum quantum numbers m_1 and m_2, as exemplified in figure 1b: this causes the bicircular trefoil to take different orientations at different azimuthal positions around the beam, and a traversal by 2π around the axis produces a rotation by a fraction

$$\gamma = \frac{m_2\omega_1 - m_1\omega_2}{\omega_1+\omega_2} = \frac{m_2 p - m_1 q}{p+q} \tag{3}$$

of a revolution. For the ω-2ω combination, with $p = 1$ and $q = 2$, this can be any arbitrary integer multiple of $1/3$; for arbitrary commensurate frequencies ω_1 and ω_2, γ can be any rational number. (Irrational γ, on the other hand, are possible by using non-commensurate frequencies, though that requires a quasi-periodic field of infinite duration.)

Moreover, once the invariance under coordinated rotations has been formulated as in equation (2), one can then solve for the most general field with that symmetry; we sketch the proof in the Methods section. When this general solution is restricted to only monochromatic contributions, one recovers the $\gamma \in \frac{1}{2}\mathbb{Z}$ constraint.

Beam topology

We have, then, beams with a trefoil polarization which rotates smoothly when moving around the axis of propagation of light in the plane perpendicular to this axis, coming back to the same trefoil but with a nontrivial internal rotation, as shown in the 'Ferris-wheel' diagram in figure 1b. For monochromatic beams, this internal rotation induces a Möbius-strip topology to the polarization [23, 32]. (This strip can also be lifted to a fully three-dimensional one if required [25, 26], but we restrict our attention to the topological Möbius strip in two dimensions.) In our case, the induced topology is different, but it can still be analysed as in the planar monochromatic case, by following the tips of the trefoil over their orbit under the transformation.

In this spirit, then, we unfold the beam's polarization as shown in figure 1c, with the beam's trefoil polarization set against the azimuthal coordinate θ, giving a corkscrew variation that terminates at a point, $\theta = 2\pi$, identical to the initial $\theta = 0$. To complete the visualization, we twist this corkscrew around to join these two equivalent points, as shown in figure 1d. Here the key information is in the path followed by the tips of the trefoil, and the details of the path of the Lissajous figure can be distilled away as in figure 1e to leave only the trefoil-tip path.

In this view it becomes clear that there is only one such path, which wraps around the figure three times before returning to its initial position; that is, all three lobe tips can be connected by the coordinated rotation. (However, this property disappears if γ is an integer.) Moreover, in this view, it becomes clear that the lobe-tip path is a curve embedded on the surface of a torus, which immediately classes it as a torus knot [42], and in the example shown, the curve is indeed knotted: within this representation, it cannot be deformed smoothly to a simple unknotted loop.

Generally speaking, a $p\omega$-$q\omega$ bicircular combination with orbital angular momenta m_1 and m_2 on the two components will similarly have the lobe tips confined to a torus surface, and the resulting torus-knot path traced by the lobe tips can be characterized by two winding numbers:

- the number $n = p+q$ of times it passes any given fixed-θ cross section of the torus, equal to the number of lobes of the Lissajous figure, and

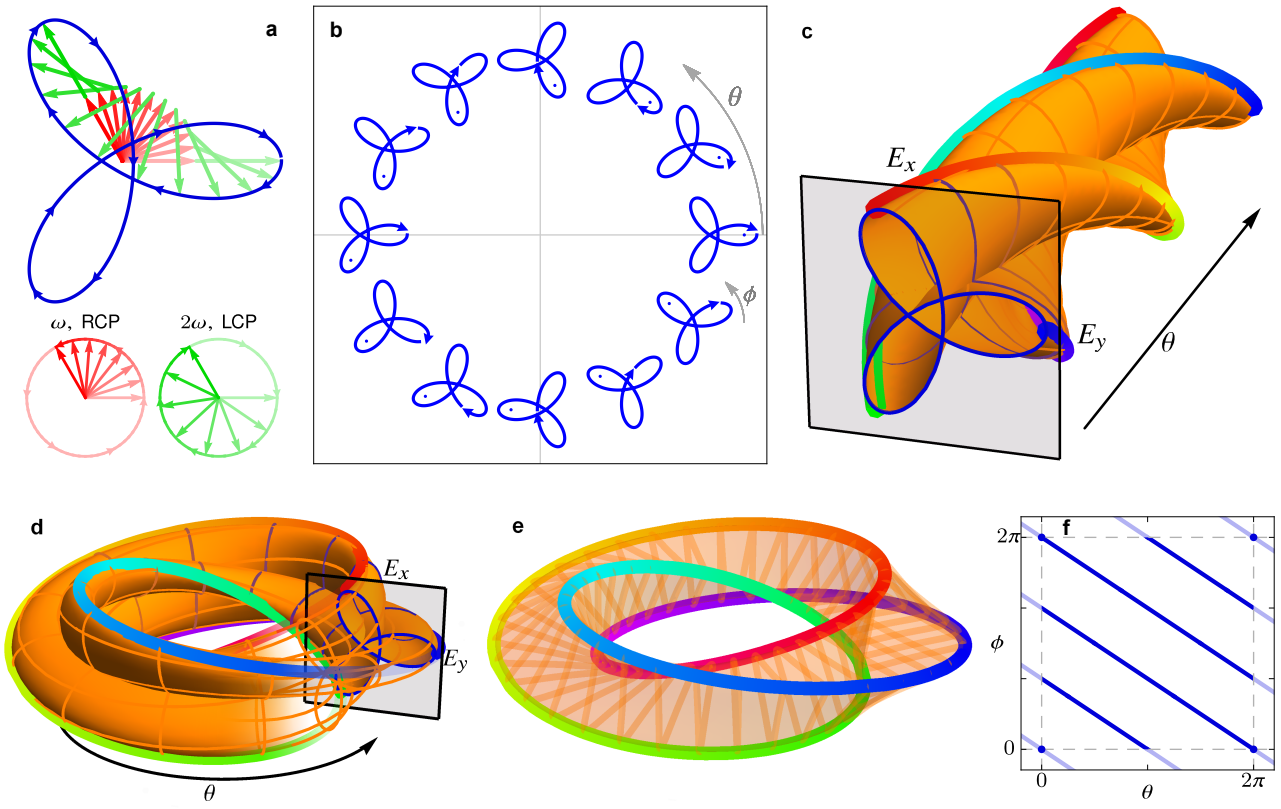

Figure 1 | Coordinated-rotation invariance and torus-knot beam topology. (a) The superposition of a right-circularly polarized beam (red) with its left-circularly polarized second harmonic (green) produces a trefoil-shaped polarization Lissajous figure (blue). The orientation of this trefoil depends on the relative phase between the two components, which can be made to vary along the azimuthal position θ by adding different orbital angular momenta m_1 and m_2 to the two components, shown in (b) for $m_1 = 0$ and $m_2 = -2$: the field then has coordinated-rotation invariance of the form $R(\gamma\alpha)\mathbf{E}(\theta - \alpha, t) = \mathbf{E}(\theta, t + \tau\alpha)$ with coordination parameter $\gamma = -2/3$ and $\tau = 1/6\omega$, and the lobe marked with a dot does not return to itself after a 2π azimuthal traversal over θ. (c) To study this field's topology, we unfold the polarization and azimuthal dependence, and then (d) twist the resulting cylinder to reconnect the planes at $\theta = 0$ and 2π. (e) If we then retain only the paths of the tips of the trefoil lobes (coloured by hue on (c-e) for visual clarity only), we obtain a knotted curve embedded on a torus, in this case the $(-2, 3)$ torus knot. (f) This torus knot can be seen as the path of the lobes on the flat torus $[0, 2\pi)\times[0, 2\pi)$ of the azimuthal and polarization angles θ and ϕ, but also as the coordinated rotations when seen as a subgroup of the independent-rotations group $\mathrm{SO}(2)\times\mathrm{SO}(2)$. 3D-printable models of (d) and (e), pictured in Fig. S1, are available in the Supplementary Material.

– the (signed) number $m = m_2 p - m_1 q$ of times it crosses the inner diameter of the torus;

the knot is then labelled as the (m, n) knot. If m and n admit a common divisor $d = \gcd(m, n)$, then the lobe-tip path separates into d separate components, each of which crosses the inner diameter m/d times; in that case, the components are $(m/d, n/d)$ torus knots pairwise linked with each other [43]. The torus-knot order (m, n), then, has the structure of a rational number, and indeed it is in direct correspondence with the rational coordination parameter $\gamma = m/n$.

This includes, in particular, the ellipse-point umbilics of the monochromatic case, whose Möbius-strip topology [23, 32] can be re-cast as the topology of the $(m, 2)$ torus knot, which then admits an immediate generalization to other members of the knot family when the monochromatic restriction is broken. In this way, our characterization in terms of torus-knot topologies forms a clear generalization of the existing classifications of the polarization singularities of monochromatic fields, and it raises broader questions about how to fully classify the polarization singularities of polychromatic fields.

The torus-knot topology of the beam also has a natural algebraic interpretation, as the symmetry subgroup of transformations, generated by $J_\gamma = \hat{L} + \gamma\hat{S}$, formed by the coordinated rotations. In paraxial optics, where the propagation axis is fixed and field polarizations can be rotated about that axis without compromising the transversality of the wave, the symmetry groups for polarization and spatial-dependence rotations decouple (or, in other words, L_z and S_z can be measured independently [11, 13]). Each of these two-dimensional rotation groups is a copy of $\mathrm{SO}(2) \cong \mathrm{U}(1)$, the circle group, which means that the full symmetry group of paraxial optics is a product of circles, $\mathrm{SO}(2)\times\mathrm{SO}(2)$, so it forms a flat torus. The coordinated rotations, for a given γ, form a one-dimensional continuous closed subgroup of that torus, which winds (m, n) times about the torus's two dimensions: in other words, it is precisely the same torus knot as the beam topology, as shown in Fig. 1f. Because of this algebraic identification to the beam topology, we refer to the subgroup generator J_γ as the torus-knot angular momentum (TKAM).

Here it is worth noting that the presence of this additional factor of SO(2), which allows the beam to store information in its internal (polarization) degree of freedom, is what allows our TKAM beams to be invariant under an angle-dependent transformation that does not return to unity after a 2π rotation,

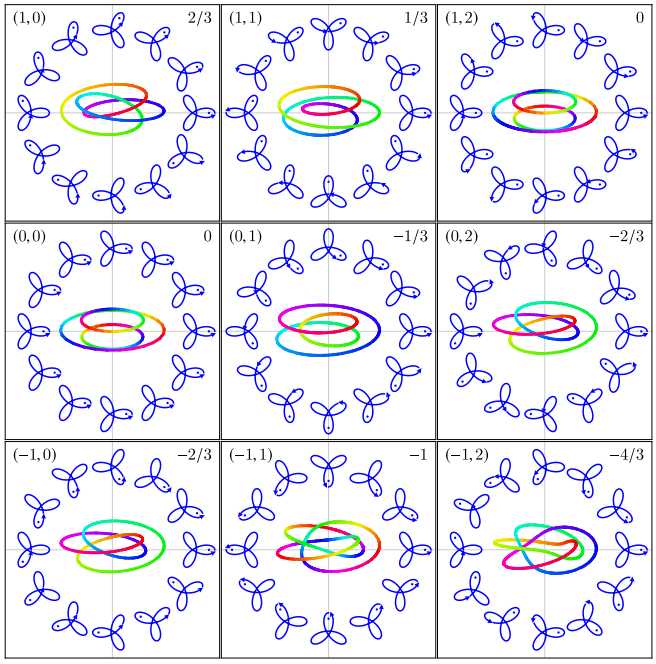

Figure 2 | Possible topologies of torus-knot beams. As the orbital angular momenta (m_1, m_2) of the ω and 2ω components is varied (upper left of each panel), the beam topology ranges over all $(m, 3)$ torus knots, and the coordination parameter γ (upper right of each panel) ranges over all multiples of $1/3$. When $m = m_2 p - m_1 q = 2m_2 - m_1$ is divisible by three, and γ is an integer, the torus knot separates into three (possibly linked), distinct rings, reflecting the fact that at $\alpha = 2\pi$ the coordinated rotation returns the trefoil lobes to their initial positions.

without incurring the discontinuities that afflict fractional-OAM beams [2, 3, 44].

More generally, torus knots have appeared several times in different optical contexts, and it is possible to form knots in this class using optical vortices [15–17], C-lines [18] and field lines [14], as explicit three-dimensional objects. Here, on the other hand, the torus knot does not exist as a real-space three-dimensional object; it is, instead, a characterization of the beam's topology as a paraxial, planar Lissajous-figure field, generalizing the Möbius-strip topology of monochromatic ellipse points.

Orientation measures and their singularities

At its heart, the optical singularity at the beam axis of a coordinated-rotation-invariant beam is a singularity in the orientation of the polarization Lissajous figure, as exemplified in Figs. 3e and 3f. As such, to fully characterize it, we need a numerical measure of this orientation. The existing orientation measures [36, 38, 39, 45] are based on the polarization matrix $\langle E_i E_j \rangle$ of the beam (with $\langle \cdot \rangle$ denoting time-averaging), but this matrix is inappropriate to the fields studied here because it is invariant under 180° rotations, and it is therefore blind to structures with three-fold or higher symmetries.

The naive extension of this approach is to change the time-averaged product of two field components for three of them: that is, the rank-three field tensor moment $\langle E_i E_j E_k \rangle$. This object is somewhat too large to analyse directly, at four independent components, but since we are looking for its transformation properties under rotations, it is natural to decompose it into the two representations it carries, $\ell = 3$ and $\ell = 1$, of the planar rotation group SO(2). Thus, the orientation of the bicircular Lissajous figure is best characterized through the multipole components

$$T_{3,3} = \left\langle \left(E_x(t) + iE_y(t)\right)^3 \right\rangle \text{ and} \tag{4a}$$

$$T_{1,3} = \left\langle \left(E_x(t) + iE_y(t)\right) \left(E_x(t)^2 + E_y(t)^2\right) \right\rangle, \tag{4b}$$

with $\alpha_3 = \frac{1}{3}\arg(T_{3,3}) \pmod{120°}$, the phase of the hexapole component, giving the trefoil orientation angle. Furthermore, the count of how many times α_3 loops about its range over a spatial traversal around the beam axis provides a new topologically-protected winding number in direct correspondence with γ. Thus, the field tensors in (4), and particularly their phase winding numbers, are stable against perturbations, and they can be used to define hexapole and dipole orientations for any arbitrary bichromatic Lissajous figure.

Here the presence of the dipole representation in (4b) is an added bonus: it provides a separate winding number, and it points to the presence of 'true' vector vortices (which cannot split into a pair of ellipse points), with a singularity in the dipole orientation angle $\alpha_1 = \arg(T_{1,3})$. This can be achieved, for example, with co-rotating circularly-polarized fields at frequencies ω and 2ω, which produces a cardioid-shaped Lissajous figure with a clear directionality.

For both field tensors, the cubic nature of the polynomial inside the time-average places strict restrictions on the field combinations that can contribute. Thus, for a bichromatic superposition of the form $\mathbf{E}(t) = \sum_{\pm} \mathrm{Re}\left[E_{1,\pm}\hat{\mathbf{e}}_{\pm}e^{-i\omega t} + E_{2,\pm}\hat{\mathbf{e}}_{\pm}e^{-2i\omega t}\right]$ with $\hat{\mathbf{e}}_{\pm} = \frac{1}{\sqrt{2}}(\hat{\mathbf{e}}_x \pm i\hat{\mathbf{e}}_y)$, the time average covers several products of exponentials, but only the ones at zero total frequency are retained: that is, products of the form $E_1^2 E_2^*$, or, more precisely,

$$T_{3,3} = \frac{3}{\sqrt{8}}\left[E_{1,-}^2 E_{2,+}^* + E_{1,+}^{*\,2} E_{2,-}\right] \tag{5}$$

for the hexapole tensor component, with the $E_1^2 E_2^*$ dependence mirroring the nonlinear processes that must be used to phase-lock the two components of the field, and which we use below to measure the trefoil orientation.

On a more general setting, the definitions in (4) generalize transparently to characterize $p\omega$-$q\omega$ combinations via the ℓ-polar component of the field tensor of rank $n = p + q$,

$$T_{\ell,n} = \left\langle \left(E_x(t) + iE_y(t)\right)^{\ell} \left(E_x(t)^2 + E_y(t)^2\right)^{\frac{n-\ell}{2}} \right\rangle. \tag{6}$$

This reproduces, via $T_{2,2}$, the existing ellipse orientation measures for the monochromatic case, and it extends to a bi-infinite family of optical topological winding numbers – which is relevant even in the ω-2ω case, where $T_{2,4}$, $T_{2,6}$ and even $T_{2,8}$ are required, on dimension-counting grounds, to fully characterize the quadrupolar orientation of general Lissajous figures. Similarly, if the polarization is taken out of the paraxial regime, the SO(3) multipole components of the field tensor are the natural arena to describe the shape of the fields and its possible singularities.

Experimental observation

The generation of bicircular ω-2ω beams with coordinated-rotation invariance is relatively simple, but their detection

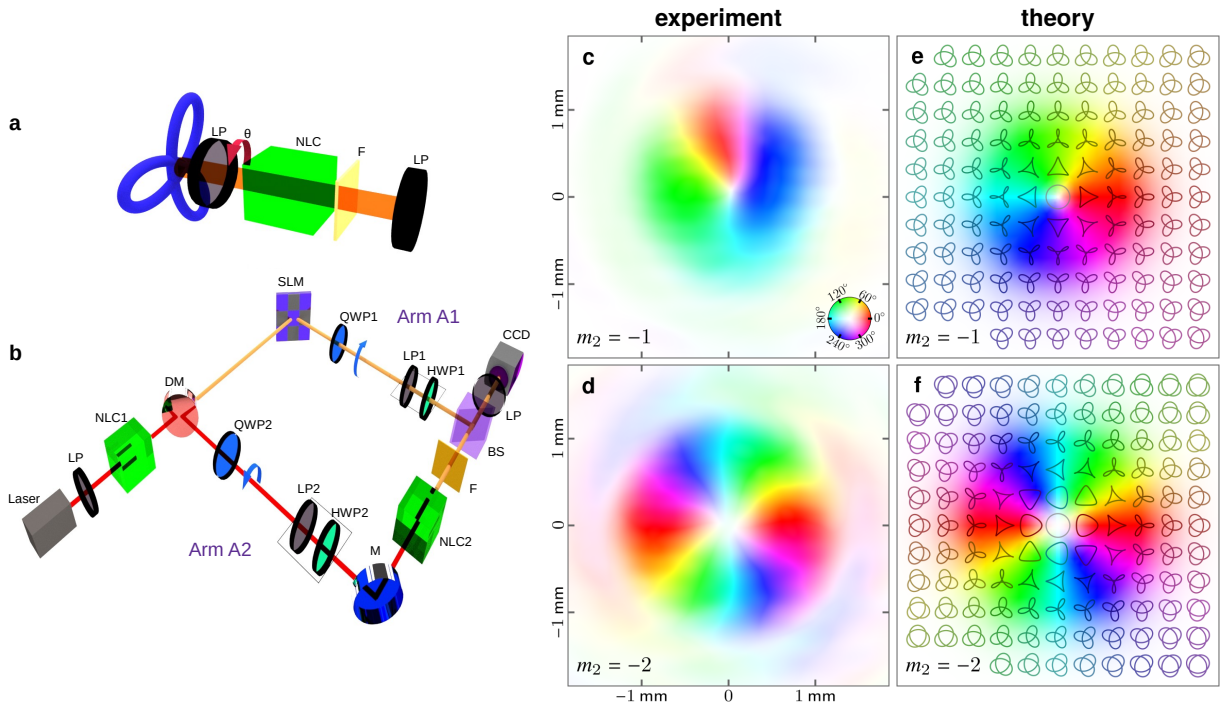

Figure 3 | Experimental configuration and results. (a) Basic scheme for nonlinear polarimetry, giving rise to (b) our experimental set-up (see the Methods section for a detailed description and definitions of the acronyms). (c,d) Experimental measurement of $T_{3,3}(x, y)$ for $m_2 = -1$ and $m_2 = -2$ on the 2ω arm, taken by Fourier-transforming the CCD images as a function of the polariser angles, with the complex phase $\arg(T_{3,3}(x, y))$ represented as the colour (i.e. the hue, given in the colour-wheel inset of panel (c)), and the amplitude $|T_{3,3}(x, y)|$ plotted as the saturation. (Similar results for other values of m_2 are presented in Fig. S5.) (e,f) Theoretical prediction for the field tensor moment $T_{3,3}(x, y)$ of a gaussian and a Laguerre-Gauss beam with $m_2 = -1$ and $m = -2$, showing a clear match to the corresponding measurements, overlaid with the Lissajous figures of the polarization at different points around the beam. At the center of the beam the Lissajous figure is a circle, and it shifts to a triangle and then a trefoil as the probe point gets further from the axis – but the orientation of the deformation away from circularity depends on the direction of departure from the axis.

poses additional challenges, since linear-optical polarimetry is insensitive to the relative phase between the two chromatic components (unless the entire beam is transformed by a physical coordinated rotation [33]), and therefore to the bicircular trefoil's orientation. To measure this phase, then, we require a nonlinear polarization tomography, with a quadratic second-harmonic-generation step that echoes the beam generation step and up-converts the phase of the fundamental so it can be compared with the second harmonic's.

For monochromatic fields, the orientation of the polarization ellipse is normally measured by inserting a linear polariser and rotating its direction θ from 0 through 2π; the orientation angle can then be extracted as the phase of the second Fourier component of the measured intensity $I(\theta)$, mirroring its appearance as the argument of the second field tensor $T_{2,2}$ (itself a traceless re-expression of the polarization matrix $\langle E_i E_j \rangle$). Similarly, for bicircular trefoils, whose orientation is encoded in $T_{3,3}$, we look for a polarimeter that will encode the bichromatic polarization as the 3θ component of the intensity as the polarimeter is rotated.

In an idealized sense, this can be achieved by projecting both colours' polarizations on a linear polariser oriented at angle θ, followed by a type 0 second-harmonic generation step on the same axis, and a filter to block the fundamental, as shown in Fig. 3a, which then feeds to an imaging system. The interference between the initial and the detection-stage 2ω light then produces a 3θ component proportional to $T_{3,3}$ – and, in addition, the first Fourier component is proportional to $T_{1,3}$. In practice, physical rotations of the quadratic crystal make for challenging alignment, so we use an optically-equivalent system sketched in Fig. 3b and described in the Methods section. We present sample experimental data and their Fourier transforms in Figs. S2, S3 and S4.

The measured Fourier components, shown in Figs. 3c and 3d, clearly exhibit a nonzero winding number, in agreement with the theoretical predictions shown in Figs. 3e and 3f. This maps directly into a nonzero winding number of the third field moment tensor $T_{3,3}$, and it acts as a smoking-gun sign of coordinated-rotation invariance with a coordination parameter γ outside the half-integral constraints of the monochromatic case.

Moreover, since it can access the relative phase between the components, this nonlinear polarization-tomography procedure can be used to reconstruct the polarization state of arbitrary bichromatic ω-2ω fields, including a full Lissajous reconstruction over the polarization singularity in our configuration. (We present a partial such reconstruction in Fig. S6.) Our approach is thus complementary to recent nonlinear-polarimetry schemes [46], providing a powerful organizing principle for those frameworks in the form of the multipolar components of Eqs. (4-6), and it constitutes, to our knowledge, the first nonlinear polarization tomography of a coherent bichromatic beam combination.

Outlook

Our results provide a set of topologies that are achievable at optical polarization singularities when the monochromatic re-

striction is lifted: beams with well-defined torus-knot angular momentum $J_\gamma = L + \gamma S$, invariant under the coordinated rotations generated by J_γ, are possible for any rational mixing parameter $\gamma = m/n$, producing a polarization field with the topology of a (m,n) torus knot. We also present the theoretical and experimental toolset, via field moment tensors and their presence in nonlinear polarization tomography, that can be used to characterize these beams and their associated singularities and winding numbers.

These features can be used as building blocks for more elaborate field topologies, from non-paraxial equivalents that can exhibit polarization torus knots as explicit three-dimensional objects as in the Möbius-band case [25, 26], to knots of coordinated-rotation-invariant vortex cores, or the trefoils' equivalent to streamlines; they can also be extended to evanescent light and combined with complex light shaping of the longitudinal polarization component [47]. The association with fractional values of an angular momentum also opens the door to the simulation of anyonic behaviour [48, 49] by using light's spin-orbit interaction with matter [29–31] and Bose-Einstein condensates [50], as well as imprinting the beam's torus-knot topology onto the state of an atomic condensate [51]. Similarly, since symmetry generators are generally conserved in nonlinear optics [37, 52, 53], the same is true for J_γ when the beams driving the process, even in highly non-perturbative interactions, are invariant under coordinated rotations, as we show in a follow-up paper [54].

From a quantum electrodynamical perspective, the existence of polychromatic beams invariant under coordinated rotations challenges the view [32] that invariant beams should be defined strictly as eigenstates of the torus-knot angular momentum generator $\hat{L} + \gamma\hat{S}$: the direct analogue to (2) is a condition of the form

$$\begin{aligned} &e^{-i\alpha(\hat{L}_z+\gamma\hat{S}_z)/\hbar}|\psi\rangle = e^{-i\tau\alpha\hat{H}/\hbar}|\psi\rangle, \text{ or equivalently} \\ &(\hat{L}_z + \gamma\hat{S}_z)|\psi\rangle = \tau\hat{H}|\psi\rangle, \end{aligned} \tag{7}$$

in its infinitesimal version. Nontrivial solutions of (7) do exist, using different numbers of photons on each component, and they have a clean relationship with the operator version of (4). However, the extent to which they can be extended to a complete basis of states requires further attention, as is the degree to which the TKAM $\hat{L}_z + \gamma\hat{S}_z$ can be considered a 'true' angular momentum operator [11, 32] when the mixing parameter γ steps out of the half-integer domain.

Acknowledgements

We thank Maria Maffei and Isaac Freund for helpful conversations, and Xavier Menino for 3D-printing assistance. E.P. acknowledges Cellex-ICFO-MPQ fellowship funding. E.P., M.L. and A.C. acknowledge funding from the Spanish Ministry MINECO (National Plan 15 Grant: FISICATEAMO No. FIS2016-79508-P, SEVERO OCHOA No. SEV-2015-0522, FPI), European Social Fund, Fundació Cellex, Generalitat de Catalunya (AGAUR Grant No. 2017 SGR 1341 and CERCA/Program), ERC AdG OSYRIS, EU FETPRO QUIC, and the National Science Centre, Poland-Symfonia Grant No. 2016/20/W/ST4/00314. V.V.H. gratefully acknowledges financial support from Secretaría de Ciencia, Tecnología e Innovación de la Ciudad de México. J.P.T. acknowledges support from Generalitat de Catalunya (Program ICREA Academia). G.J.M. was supported by the Secretaria d'Universitats i Recerca del Departament d'Economia i Coneixement de la Generalitat de Catalunya, as well as the European Social Fund – FEDER. A.P. acknowledges funding from Comunidad de Madrid through TALENTO grant ref. 2017-T1/IND-5432. A.C. acknowledges financial support from the ERC Synergy Grant UQUAM, the SFB FoQuS (FWF Project No. F4016-N23), the UAB Talent Research program and from the Spanish Ministry of Economy and Competitiveness under Contract No. FIS2017-86530-P.

Author contributions

E.P. conceived the project and developed the theory. G.J., V.V.H, E.P. and J.P.T. designed the experiment. G.J. and V.V.H. conducted the experiment. A.P., A.C. and M.L. assisted with the theory. E.P. wrote the manuscript, with assistance from V.V.H. on the Methods section. J.P.T. supervised the experimental work; M.L. oversaw the theory development. All authors contributed to the scientific discussion.

References

[1] J. P. Torres and L. Torner (eds.). *Twisted Photons: Applications of Light with Orbital Angular Momentum* (Wiley, Weinheim, 2011).

[2] D. L. Andrews and M. Babiker (eds.). *The Angular Momentum of Light* (Cambridge University Press, Cambridge, 2012).

[3] G. Gbur. *Singular optics* (CRC Press, Boca Raton, 2016).

[4] H. Rubinsztein-Dunlop et al. Roadmap on structured light. *J. Opt.* **19** no. 1, p. 013 001 (2017). UPC eprint.

[5] J. F. Nye and M. V. Berry. Dislocations in wave trains. *Proc. R. Soc. A* **336** no. 1605, pp. 165–190 (1974). Author eprint.

[6] J. Wang et al. Terabit free-space data transmission employing orbital angular momentum multiplexing. *Nature Photon.* **6** no. 7, pp. 488–491 (2012). TAU eprint.

[7] S. Fürhapter et al. Spiral phase contrast imaging in microscopy. *Opt. Express* **13** no. 3, pp. 689–694 (2005).

[8] V. Garcés-Chávez et al. Transfer of orbital angular momentum to an optically trapped low-index particle. *Phys. Rev. A* **66** no. 6, p. 063 402 (2002). UNAM eprint.

[9] M. Padgett and R. Bowman. Tweezers with a twist. *Nature Photon.* **5** no. 6, pp. 343–348 (2011).

[10] C. Hernández-García et al. Generation and applications of extreme-ultraviolet vortices. *Photonics* **4** no. 2, p. 28 (2017).

[11] S. M. Barnett et al. On the natures of the spin and orbital parts of optical angular momentum. *J. Opt.* **18** no. 6, p. 064 004 (2016).

[12] G. Molina-Terriza, J. P. Torres and L. Torner. Twisted photons. *Nature Phys.* **3** no. 5, pp. 305–310 (2007).

[13] S. Van Enk and G. Nienhuis. Spin and orbital angular momentum of photons. *Europhys. Lett.* **25** no. 7, pp. 497–501 (1994).

[14] H. Kedia et al. Tying knots in light fields. *Phys. Rev. Lett.* **111** no. 15, p. 150 404 (2013). arXiv:1302.0342.

[15] J. Leach et al. Laser beams: Knotted threads of darkness. *Nature* **432** no. 7014, p. 165 (2004).

[16] M. R. Dennis et al. Isolated optical vortex knots. *Nature Phys.* **6** no. 2, pp. 118–121 (2010).

[17] D. Sugic and M. R. Dennis. Knotted hopfion in tightly focused light. In L. Marrucci (ed.), *Proceedings of the 4th International Conference on Optical Angular Momentum* (Jean Gilder, 2017), p. 137.

[18] H. Larocque et al. Reconstructing the topology of optical polarization knots. *Nature Phys.* **14** no. 11, p. 1079 (2018). author eprint.

[19] I. Freund. Cones, spirals, and Möbius strips, in elliptically polarized light. *Opt. Commun.* **249** no. 1-3, pp. 7–22 (2005).

[20] J. F. Nye and J. V. Hajnal. The wave structure of monochromatic electromagnetic radiation. *Proc. R. Soc. Lond., Ser. A* **409** no. 1836, pp. 21–36 (1987). JSTOR:2398191.

[21] M. R. Dennis. Polarization singularities in paraxial vector fields: morphology and statistics. *Opt. Commun.* **213** no. 4–6, pp. 201–221 (2002). Southampton eprint.

[22] T. Bauer et al. Multi-twist polarization ribbon topologies in highly-confined optical fields (2019). arXiv:1901.11337.

[23] I. Freund. Optical Möbius strips in three-dimensional ellipse fields: I. Lines of circular polarization. *Opt. Commun.* **283** no. 1, pp. 1–15 (2010). arXiv:0903.2927.

[24] I. Freund. Optical Möbius strips in three-dimensional ellipse fields: II. Lines of circular polarization. *Opt. Commun.* **283** no. 1, pp. 16–28 (2010). arXiv:0905.3364.

[25] T. Bauer et al. Observation of optical polarization Möbius strips. *Science* **347** no. 6225, pp. 964–966 (2015). Rochester U eprint.

[26] T. Bauer et al. Optical polarization Möbius strips and points of purely transverse spin density. *Phys. Rev. Lett.* **117** no. 1, p. 013 601 (2016). arXiv:1601.06072.

[27] E. J. Galvez et al. Multitwist Möbius strips and twisted ribbons in the polarization of paraxial light beams. *Sci. Rep.* **7**, p. 13 653 (2017).

[28] A. Garcia-Etxarri. Optical polarization Möbius strips on all-dielectric optical scatterers. *ACS Photonics* **4** no. 5, pp. 1159–1164 (2017).

[29] F. Cardano and L. Marrucci. Spin–orbit photonics. *Nature Photon.* **9** no. 12, pp. 776–778 (2015).

[30] K. Y. Bliokh et al. Spin–orbit interactions of light. *Nature Photon.* **9** no. 12, pp. 796–808 (2015). arXiv:1505.02864.

[31] K. Y. Bliokh. Geometrodynamics of polarized light: Berry phase and spin Hall effect in a gradient-index medium. *J. Opt. A: Pure Appl. Opt.* **11** no. 9, p. 094 009 (2009). arXiv:0903.1910.

[32] K. E. Ballantine, J. F. Donegan and P. R. Eastham. There are many ways to spin a photon: Half-quantization of a total optical angular momentum. *Sci. Adv.* **2** no. 4, p. e1501 748 (2016).

[33] J. Leach et al. Interferometric methods to measure orbital and spin, or the total angular momentum of a single photon. *Phys. Rev. Lett.* **92** no. 1, p. 013 601 (2004).

[34] E. Galvez et al. Interferometric measurement of the helical mode of a single photon. *New J. Phys.* **13** no. 5, p. 053 017 (2011).

[35] D. A. Kessler and I. Freund. Lissajous singularities. *Opt. Lett.* **28** no. 2, pp. 111–113 (2003).

[36] I. Freund. Bichromatic optical Lissajous fields. *Opt. Commun.* **226** no. 1–6, pp. 351–376 (2003).

[37] A. Fleischer et al. Spin angular momentum and tunable polarization in high-harmonic generation. *Nature Photon.* **8** no. 7, pp. 543–549 (2014). arXiv:1310.1206.

[38] I. Freund. Polychromatic polarization singularities. *Opt. Lett.* **28** no. 22, pp. 2150–2152 (2003).

[39] I. Freund. Polarization critical points in polychromatic optical fields. *Opt. Commun.* **227** no. 1, pp. 61–71 (2003).

[40] H. Yan and B. Lü. Dynamical evolution of Lissajous singularities in free-space propagation. *Phys. Lett. A* **374** no. 35, pp. 3695–3700 (2010).

[41] C. Haitao, Z. Gao and W. Wang. Propagation of the Lissajous singularity dipole emergent from non-paraxial polychromatic beams. *Opt. Commun.* **393**, pp. 17–24 (2017). See also references therein.

[42] C. C. Adams. *The Knot Book: An elementary introduction to the mathematical theory of knots* (American Mathematical Society, Providence, Rhode Island, 2004).

[43] D. Rolfsen. *Knots and Links* (American Mathematical Society, Providence, Rhode Island, 2003), pp. 17–18.

[44] J. B. Götte et al. Light beams with fractional orbital angular momentum and their vortex structure. *Opt. Express* **16** no. 2, pp. 993–1006 (2008). U Glasgow eprint.

[45] I. Freund. Coherency matrix description of optical polarization singularities. *J. Opt. A: Pure Appl. Opt.* **6** no. 5, p. S229 (2004).

[46] M. Samim, S. Krouglov and V. Barzda. Nonlinear Stokes-Mueller polarimetry. *Phys. Rev. A* **93** no. 1, p. 013 847 (2016). arXiv:1510.02410.

[47] F. Maucher et al. Creating complex optical longitudinal polarization structures. *Phys. Rev. Lett.* **120** no. 16, p. 163 903 (2018). arXiv:1801.05668.

[48] F. Wilczek. Quantum mechanics of fractional-spin particles. *Phys. Rev. Lett.* **49** no. 14, pp. 957–959 (1982).

[49] D. Arovas, J. R. Schrieffer and F. Wilczek. Fractional statistics and the quantum hall effect. *Phys. Rev. Lett.* **53** no. 7, pp. 722–723 (1984).

[50] Y.-J. Lin, K. Jiménez-García and I. B. Spielman. Spin–orbit-coupled Bose–Einstein condensates. *Nature* **471** no. 7336, pp. 83–86 (2011). arXiv:1103.3522.

[51] F. Maucher, S. A. Gardiner and I. G. Hughes. Excitation of knotted vortex lines in matter waves. *New J. Phys.* **18** no. 6, p. 063 016 (2016).

[52] N. Bloembergen. Conservation laws in nonlinear optics. *J. Opt. Soc. Am.* **70** no. 12, pp. 1429–1436 (1980).

[53] D. D. Hickstein et al. Non-collinear generation of angularly isolated circularly polarized high harmonics. *Nature Photon.* **9** no. 11, pp. 743 – 750 (2015). JILA eprint.

[54] E. Pisanty et al. Conservation of torus-knot angular momentum in high-order harmonic generation. *Phys. Rev. Lett.* **122** no. 20, p. 203 201 (2019). arXiv:1810.06503.

[55] E. Pisanty. LISSAFIRE: Lissajous-Figure Reconstruction for nonlinear polarization tomography of bichromatic fields. `https://github.com/episanty/LISSAFIRE`, v1.0.2 (2019).

[56] E. Pisanty et al. Code and data for 'Knotting fractional- order knots with the polarization state of light'. doi:10.5281/zenodo.2649391 (Zenodo, 2019).

[57] See the Supplementary Material at doi:10.5281/zenodo.2597667 for 3D-printable models of Figs. 1d and 1e.

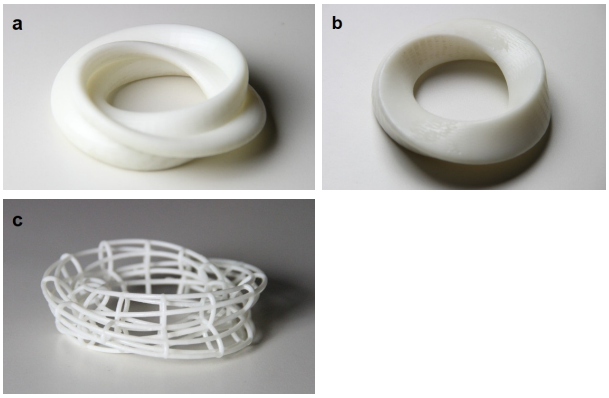

Figure S1 | 3D prints of the torus-knot topology. Models of the torus-knot beam topology of Fig. 1, available at Ref. 57, printed in 3D using resin-based stereolithography on a Formlabs Form 2 printer. 3D Prints: Xavier Menino (ICFO); Image Credits: © ICFO.

Methods

General solution to the invariance equation

In this section we show the general solution to the field invariance property (2) under coordinated rotations,

$$R(\gamma\alpha)\mathbf{E}\big(R^{-1}(\alpha)\mathbf{r},t\big) = \mathbf{E}(\mathbf{r},t+\tau\alpha), \tag{2}$$

where the rotation matrix acts as

$$R(\alpha)\mathbf{v} = \begin{pmatrix}\cos(\alpha) & -\sin(\alpha) & 0\\ \sin(\alpha) & \cos(\alpha) & 0\\ 0 & 0 & 1\end{pmatrix}\begin{pmatrix}v_x\\ v_y\\ v_z\end{pmatrix}, \tag{8}$$

so its action as a passive transformation in cylindrical coordinates is $\mathbf{E}(R(\alpha)^{-1}\mathbf{r},t) = \mathbf{E}(r,\theta-\alpha,z,t)$. With that in hand, we can turn the invariance property (2) into its local version by differentiating with respect to α, which produces

$$\begin{cases} -\dfrac{\partial E_x}{\partial\theta} - \gamma E_y = \tau\dfrac{\partial E_x}{\partial t}, & \text{(9a)}\\ -\dfrac{\partial E_y}{\partial\theta} + \gamma E_x = \tau\dfrac{\partial E_y}{\partial t}. & \text{(9b)}\end{cases}$$

This is a pair of coupled partial differential equations, but since the derivatives appear with the same sign in both, we can reduce them to a single unified form by setting $u = \theta + t/\tau$ and $v = \theta - t/\tau$, so that they combine to a single complex equation,

$$\left(-\frac{\partial}{\partial u} + \frac{1}{2}i\gamma\right)(E_x + iE_y) = 0, \tag{10}$$

where the conjugate coordinate v drops out, leading to the simple solution

$$\begin{aligned} E_x + iE_y &= F(v)e^{\frac{i}{2}\gamma u} && \text{(11a)}\\ &= F(\theta - t/\tau)e^{\frac{1}{2}i\gamma(\theta+t/\tau)} && \text{(11b)}\end{aligned}$$

in terms of an arbitrary function $F(v) = F(\theta - t/\tau)$.

The solution in (11), however, is not quite complete, because of the possible fractional exponent in $e^{\frac{1}{2}i\gamma(\theta+t/\tau)}$, in a function that needs to be periodic in θ, and this needs to be offset by setting $F(v) = \tilde{F}(v)e^{-\frac{1}{2}i\gamma v}$ for a periodic $\tilde{F}(v)$. This then requires that the solution be of the form

$$\begin{aligned} E_x + iE_y &= \tilde{F}(\theta - t/\tau)e^{i\gamma t/\tau} && \text{(12a)}\\ &= \sum_{m=-\infty}^{\infty} F_m e^{im\theta}e^{i\frac{\gamma-m}{\tau}t}, && \text{(12b)}\end{aligned}$$

in terms of the Fourier coefficients of $\tilde{F}(v)$. This completely fixes the possible dependence of $\mathbf{E}$, as a superposition of a discrete set of orbital angular momentum (OAM) modes $e^{im\theta}$ at prescribed frequencies $\left|\frac{\gamma-m}{\tau}\right|$, with right- (resp. left-)handed circular polarizations at negative (resp. positive) frequencies.

In particular, the general solution in (12) is enough to reproduce the restrictions of the monochromatic case, which only allows for two terms m_1 and m_2 to contribute to the sum, at positive and negative frequencies $e^{-i\omega t}$ and $e^{+i\omega t}$, which then requires that

$$\frac{\gamma - m_1}{\tau} = \omega = -\frac{\gamma - m_2}{\tau}, \tag{13}$$

and therefore restricts the coordination parameter

$$\gamma = \frac{m_1 + m_2}{2} \tag{14}$$

to integer or half-integer values, as found in previous work.

On the other hand, if the general solution (12) is required to include right- and left-handed components with OAM m_1 and m_2 at frequencies ω_1 and ω_2, then γ and τ are required to obey $\gamma + m_1 = \omega_1\tau$ and $\gamma - m_2 = -\omega_2\tau$, resulting in the arbitrary coordination parameter γ given in (3), together with the delay constant $\tau = \frac{m_1+m_2}{\omega_1+\omega_2}$.

Nonlinear polarization tomography

In this section we present the core mechanism for nonlinear polarization tomography of bichromatic ω-2ω combinations, as schematized in Fig. 3a; we consider its effect on an arbitrary bichromatic combination, but we neglect the spatial dependence for now. Thus, we consider an electric field of the form

$$\mathbf{E}(t) = \mathrm{Re}\big[\mathbf{E}_1 e^{-i\omega t} + \mathbf{E}_2 e^{-2i\omega t}\big], \tag{15}$$

which then passes through

1. a linear polariser along $\hat{\mathbf{u}} = \cos(\theta)\hat{\mathbf{e}}_x + \sin(\theta)\hat{\mathbf{e}}_y$, which transforms the field to

$$\mathrm{LP}_\theta\mathbf{E}(t) = \hat{\mathbf{u}}\,\mathrm{Re}\big[\hat{\mathbf{u}}\cdot\mathbf{E}_1 e^{-i\omega t} + \hat{\mathbf{u}}\cdot\mathbf{E}_2 e^{-2i\omega t}\big]; \tag{16}$$

followed by

2. a nonlinear crystal that produces type 0 second-harmonic generation along $\hat{\mathbf{u}}$, thereby adding a contribution

$$\mathbf{E}_{\mathrm{SHG}}(t) = \hat{\mathbf{u}}\,\mathrm{Re}\big[\chi\,(\hat{\mathbf{u}}\cdot\mathbf{E}_1)^2\,e^{-2i\omega t}\big] \tag{17}$$

to the field, where χ is a combination of the crystal's quadratic susceptibility and the interaction length; and finally

3. a filter that eliminates the fundamental before the intensity is measured.

Our core observable is therefore the measured intensity as a function of the rotation angle θ, given by the time average

$$I(\theta) = \left\langle \mathrm{Re}\left[\chi\,(\hat{\mathbf{u}}\cdot\mathbf{E}_1)^2\,e^{-2i\omega t} + \hat{\mathbf{u}}\cdot\mathbf{E}_2 e^{-2i\omega t}\right]^2\right\rangle$$
$$= \frac{1}{2}\left[(\chi\,(\hat{\mathbf{u}}\cdot\mathbf{E}_1^*)^2 + \hat{\mathbf{u}}\cdot\mathbf{E}_2^*)(\chi\,(\hat{\mathbf{u}}\cdot\mathbf{E}_1)^2 + \hat{\mathbf{u}}\cdot\mathbf{E}_2)\right]. \quad (18)$$

Writing the electric field in circular components as $\mathbf{E}_j = \sum_\pm E_{j,\pm}\hat{\mathbf{e}}_\pm$ with $\hat{\mathbf{e}}_\pm = \frac{1}{\sqrt{2}}(\hat{\mathbf{e}}_x \pm i\hat{\mathbf{e}}_y)$ and $j = 1,2$, as in the main text, so that the components along $\hat{\mathbf{u}}$ now read $\hat{\mathbf{u}}\cdot\mathbf{E}_j = \frac{1}{\sqrt{2}}\left(E_{j,+}e^{i\theta} + E_{j,-}e^{-i\theta}\right)$, we can express the intensity as an explicit Fourier series of the form

$$I(\theta) = I_0 + I_1(\theta) + I_2(\theta) + I_3(\theta) + I_4(\theta). \quad (19)$$

Here the even components, I_0, $I_2(\theta)$ and $I_4(\theta)$, carry limited information, as they contain no cross terms between $\mathbf{E}_1$ and $\mathbf{E}_2$, and they are therefore insensitive to the coherence between the two components:

$$I_0 = \frac{1}{8}\chi^2\left(|\mathbf{E}_1|^4 + 2\left|E_{1,-}E_{1,+}\right|^2\right) + \frac{1}{4}|\mathbf{E}_2|^2, \quad (20a)$$

$$I_2(\theta) = \mathrm{Re}\left[\left(\frac{1}{2}\chi^2|\mathbf{E}_1|^2E_{1,-}^*E_{1,+} + \frac{1}{2}E_{2,-}^*E_{2,+}\right)e^{2i\theta}\right], \quad (20b)$$

$$I_4(\theta) = \mathrm{Re}\left[\frac{1}{4}\chi^2E_{1,-}^{*\,2}E_{1,+}^2e^{4i\theta}\right]. \quad (20c)$$

The odd components, $I_1(\theta)$ and $I_3(\theta)$, on the other hand, do contain the necessary $\mathbf{E}_1$-$\mathbf{E}_2$ coherences: they are given by

$$I_1(\theta) = \frac{\chi}{\sqrt{8}}\,\mathrm{Re}\Big[\Big(E_{1,+}^*\left(\mathbf{E}_1^*\cdot\mathbf{E}_2 + E_{1,-}^*E_{2,-}\right) + E_{1,-}\left(\mathbf{E}_1\cdot\mathbf{E}_2^* + E_{1,+}E_{2,+}^*\right)\Big)^* e^{i\theta}\Big] \quad (20d)$$

$$I_3(\theta) = \frac{\chi}{\sqrt{8}}\,\mathrm{Re}\left[\left(E_{1,-}^2E_{2,+}^* + E_{1,+}^{*\,2}E_{2,-}\right)^* e^{3i\theta}\right] \quad (20e)$$

and, in fact, they are direct measures of the dipole and hexapole components of the third field moment tensor, as defined in (4), which are given in this context by

$$T_{3,3} = \frac{3}{\sqrt{8}}\left[E_{1,-}^2E_{2,+}^* + E_{1,+}^{*\,2}E_{2,-}\right] \quad \text{and} \quad (21a)$$

$$T_{1,3} = \frac{1}{\sqrt{8}}\left[E_{1,+}^*\left(\mathbf{E}_1^*\cdot\mathbf{E}_2 + E_{1,-}^*E_{2,-}\right) + E_{1,-}\left(\mathbf{E}_1\cdot\mathbf{E}_2^* + E_{1,+}E_{2,+}^*\right)\right]. \quad (21b)$$

The output of this polarization tomography, then, is the set of Fourier coefficients over θ, $J_0 = I_0 \geq 0$ and $I_n = 2\,\mathrm{Re}(J_n e^{in\theta})$ for $|n| \geq 1$, so that the set $\{J_0, J_1, J_2, J_3, J_4\}$ comprises a total of nine real-valued parameters. On the other hand, the inputs to that calculation, $\{E_{1,+}, E_{1,-}, E_{2,+}, E_{2,-}\}$, occupy the eight-dimensional space $\mathbb{C}^4$, and one of those eight dimensions is lost to a partial degeneracy of the $\{E_{j,\pm}\} \mapsto \{J_n\}$ mapping, which is not affected by a transformation of the form $(\mathbf{E}_1, \mathbf{E}_2) \mapsto (e^{i\varphi}\mathbf{E}_1, e^{2i\varphi}\mathbf{E}_1)$. This means, in turn, that the $\{J_0, J_1, J_2, J_3, J_4\}$ can only occupy, at most, a seven-dimensional submanifold of their nine-dimensional ambient space: in other words, the polarimetry data $\{J_n\}$ contain, in principle, enough information to reconstruct the electric field amplitudes of both beams.

The mapping itself, $\{E_{j,\pm}\} \mapsto \{J_n\}$ as per Eqs. (20), is a complicated polynomial of third and fourth degree, in eight variables, so it cannot easily be inverted directly. For simulated data, it is straightforward to find a field-amplitude preimage $\{E_{j,\pm}\}$ via least-squares minimization on the $\{J_n\}$. For the experimental data, however, which are subject to noise (probably from interferometric drift), this least-squares minimization procedure finds multiple local minima, and these require additional information to be discarded safely; moreover, the presence of noise produces some amount of 'leakage' of signal between the two components. Nevertheless, our existing data do permit a partial reconstruction of the field amplitudes and therefore of the experimental Lissajous field (modulo the assumption that $\chi = 1$, absent a detailed measurement of the detection-stage harmonic generation efficiency), and we present one such partial reconstruction in Fig. S6; our implementation of the reconstruction algorithm is available at Ref. 55. Future work aims at improving this measurement.

Experimental implementation

We now describe our experimental implementation of the abstract nonlinear polarimetry delineated above, embodied in the Mach-Zehnder interferometer depicted in Fig. 3b.

We used as the pump source a Gaussian beam from a diode laser amplified with an erbium-doped fibre amplifier (EDFA), centred at 1550 nm with a power of 300 mW, a beam diameter of 2.6 mm and vertical polarization, which is oriented using a linear polarizer (LP). The pump beam was sent through a lens L_1 (we omit all lenses from Fig. 3b for clarity), with a focal length of 15 cm, pumping a 10-mm-long periodically-poled lithium niobate (PPLN) nonlinear crystal (NLC1) which was placed at the focal distance of L_1 to generate second harmonic type 0 centred at 775 nm. A dichroic mirror (DM) was placed after the NLC1, which transmits the light centred at 775 nm from the second-harmonic generation and reflected the light centred at 1550 nm from the pump, forming the two arms of the Mach-Zehnder interferometer.

The beam with wavelength centred at 775 nm was propagated trough the arm A1 and transmitted through the lens L_2, with focal length of $f = 20$ cm, forming a telescope with lens L_1 to magnify the beam by a factor of $\sim \times 1.33$.

In order to turn this beam into a high-quality higher-order Laguerre-Gauss Beam (LGB) we used a Spatial Light Modulator (SLM, Hamamatsu X10468-2, 792 × 600 pixels with pixel pitch of 20 µm) so as to modulate phase of the incoming beam by phase patterns for LGB displayed on the SLM. A half-wave plate HWP (not shown) was used to change the polarization orientation of the beam to horizontal, as required by the SLM, and another HWP (not shown) was used return the reflected beam to vertical polarization. The output beam is a high-quality LGB with vertical polarization, with a topological charge m_2 controlled by the phase winding on the SLM.

Following the dichroic mirror DM, the beam centred at 1550 nm was reflected and propagated along the arm A2. First it was transmitted through a lens L_3 with focal length of $f = 15$ cm which forms a telescope with the lens L_1 with magnification ×1 to collimate the beam.

In order to obtain counter-rotating circular polarizations on both beams, a quarter-wave plate was placed in each arm, so that along the arm A1 and just after the SLM our LGB was

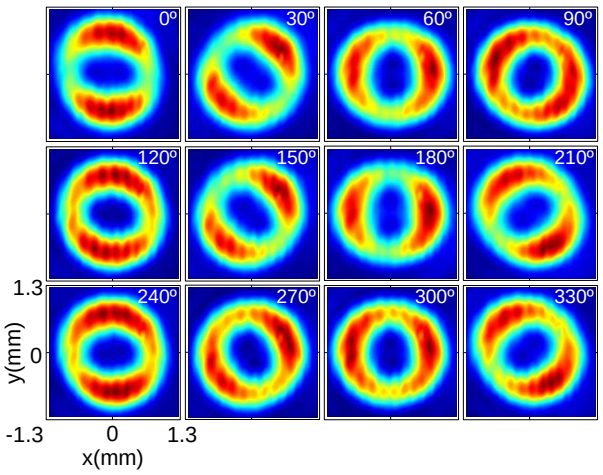

Figure S2 | Observed interference patterns. Representative interference patterns observed with $m_2 = -2$ for various values of the polariser angle θ.

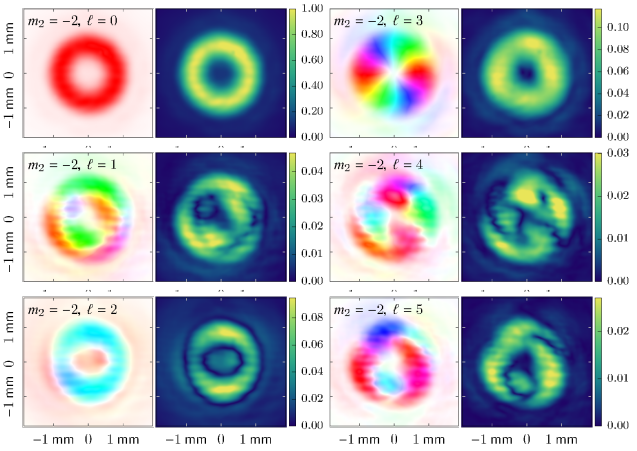

Figure S3 | Transformed experimental results. Fourier transform of the experimental results of Fig. S2, shown in both magnitude (right-hand panels) and phase (left-hand panels; $\arg(\tilde{f}_\ell(x,y))$ as the hue and $|\tilde{f}_\ell(x,y)|$ as the saturation). We normalize $|\tilde{f}_\ell(x,y)|$ to its maximum value within each plot, but we show its scale with respect to the base $\ell = 0$ intensity $|\tilde{f}_0(x,y)|$ on the density-plot tick marks. Thus, the only meaningful channel with $\ell > 0$ is $\ell = 3$, with a dominant signal and a clear phase winding.

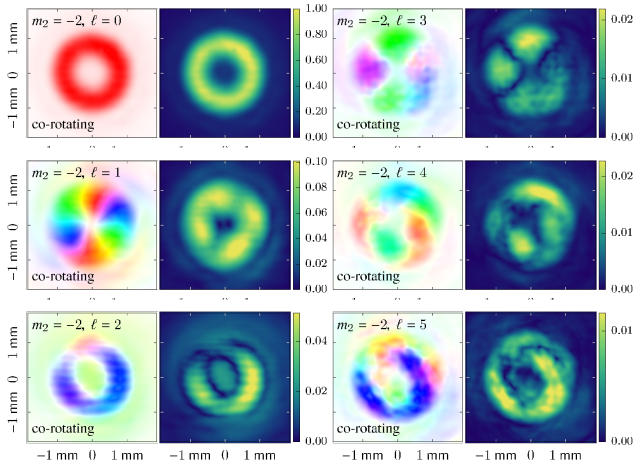

Figure S4 | Transformed experimental results. Analysis of the results, as in Fig. S3, for co-rotating circular polarizations on both arms of the interferometer, with $m_2 = -2$. Here the dominant component shifts from $\ell = 3$ to $\ell = 1$, showing a nonzero phase winding on $T_{1,3}$, and with that a 'true' vector vortex.

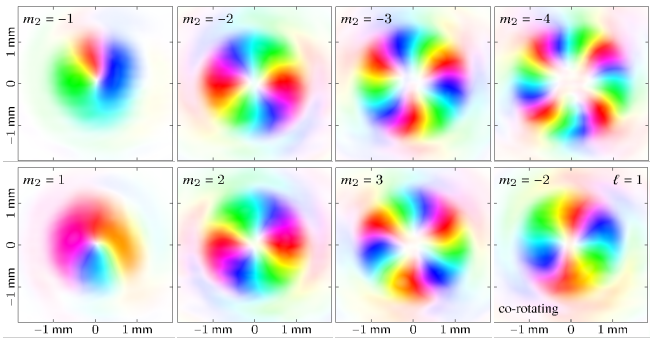

Figure S5 | Observed phase vortices. Experimentally-observed phase vortices, in $T_{3,3}$ plotted as in Figs. 3, S3 and S4, for different values of the second harmonic's OAM m_2, as well as for the co-rotating case of Fig. S4.

transmitted through the quarter-wave plate QWP1 oriented at 45°, also along the arm A2 and just after the DM the beam with wavelength centred at 1550 nm was transmitted through the quarter-wave plate QWP2 oriented at −45°.

For the detection stage, both beams are transmitted through a linear polariser LP1 and LP2, for each arm A1 and A2 respectively, to project the polarization state at angle θ. We keep the detection nonlinear crystal (NLC2, 10-mm-long PPLN) stationary, to ensure stable phase-matching, rotating the polarization after LP1 and LP2 into its phase-matching angle using half-wave plates HWP1 and HWP2 at angles $\theta/2$. The NLC2 crystal was placed in the arm A2 between the lenses L_4 and L_5, with focal lengths of $f = 15$ cm and $f = 30$ cm respectively, so as to magnify the beam by a factor of $\sim\times 2$. Pump light was eliminated using a bandpass filter (F) centred at 775 nm with a bandwidth of 10 nm. The two beams were recombined by a beamsplitter and their interference pattern was observed with a CCD camera (resolution of 1200×1600 pixels, pixel width 4.4 µm).

We recorded data by imaging the interference patterns produced by setting the linear polariser angles θ (and with them the half-wave plate angles $\theta/2$) between $\theta = 0°$ and $\theta = 330°$ in steps of 30°, which produces a rigid rotation on the interference pattern as shown in Fig. S2. To complete the polarization tomography, we Fourier transform the $N = 12$ measured images $f_{\theta_j}(x,y)$, over $\theta_j = 2\pi j/N$ with $j = 0, 1, \ldots, N-1$, to $\tilde{f}_\ell(x,y) = \sum_{j=0}^{N-1} e^{i\ell\theta_j} f_{\theta_j}(x,y)$; we show a representative example in Fig. S3. Generally, there is some residual signal on most components, but only the dominant channel at $\ell = 3$ carries a nonzero phase winding. We collect all the observed nontrivial phase vortices in Fig. S5.

A similar analysis carried out with co-rotating polarizations on both arms (achieved by setting QWP2 to +45°), shown in Fig. S4, exhibits a shift in the dominant Fourier component from $\ell = 3$ to $\ell = 1$, with a nonzero phase winding on the latter, corresponding to the observation of a phase singularity in the dipole field moment $T_{1,3}$.

Data and code availability

The data from the experiment, together with the scripts for generating the experimental figures and the code used for producing the theoretical figures, has been publicly archived

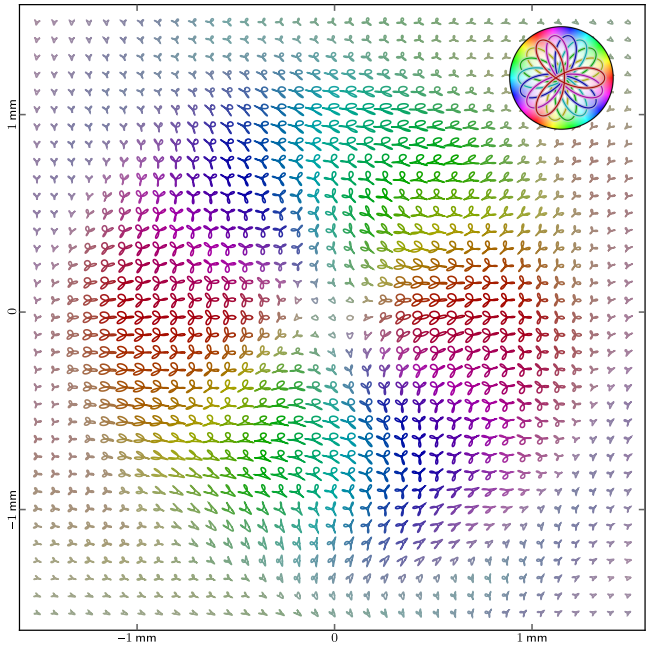

Figure S6 | Reconstruction of Lissajous-figure fields. Reconstruction of the trefoil Lissajous figures from the experimental data at $m = -2$ shown in Fig. 3d, via the least-squares minimization procedure described in Methods, and assuming unit conversion efficiency χ on NLC2. The figures exhibit some distortion, probably due to interferometric drift over the data collection, which also induces some amount of cross-talk between the reconstructed $\mathbf{E}_1$ and $\mathbf{E}_2$ fields (for which evaluating the uncertainty requires further analysis); despite this distortion, the $\gamma = -2/3$ rotation coordination parameter of the trefoil lobes over an azimuthal traversal is clearly visible. The figures are coloured according to their three-fold orientation angle, $\alpha_3 = \frac{1}{3}\arg(T_{3,3}) \pmod{120°}$, with $T_{3,3}$ taken from the Fourier-transformed experimental data, as shown in the inset.

in Ref. 56, at the Zenodo repository doi:10.5281/zenodo.2649391.